Contents lists available at ScienceDirect

Results in Optics

Wide field-of-view Fourier Ptychography microscopy based on Fresnel propagation scheme

Mojde Hasanzade [a,*], Dag Werner Breiby [a,b], Muhammad Nadeem Akram [a,*]

[a] *Department of Microsystems, University of South-Eastern Norway, Raveien 215, Borre, Norway*
[b] *PoreLab, Department of Physics, Norwegian University of Science and Technology(NTNU), Høgskoleringen 5, 7491 Trondheim, Norway*

ARTICLE INFO

ABSTRACT

Fourier ptychographic microscopy (FPM) is a computational imaging method that gives a significantly increased space-bandwidth product, in practice high resolution combined with a wide field of view. In this article, we propose an improved Fourier Ptychography algorithm based on Fresnel wave propagation integral for wide field-of-view coherent imaging while correcting for the misalignment of the illuminating LED board and calibration of system parameters. In addition, the wave emanating from the LEDs is taken to be parabolic instead of plane wave as done by others. The advantage of this scheme is that it enables to simulate the transition regions between bright and dark field in wide image patches, and hence this feature can be used to estimate the LED misalignment as well as the distortion of the imaging lens. Experimental results are presented for a USAF resolution target and a biological sample for on-axis and off-axis image patches over a wide sample area showing excellent performance of this scheme when compared to the traditional Fraunhofer-model based Fourier Ptychography algorithm. The article summarizes with high technical detail our experiences with developing and implementing improved FPM methods and will hopefully assist other scientists entering this scientific field.

1. Introduction

Fourier Ptychography microscopy (FPM) is becoming a well-known coherent imaging technique for increasing the overall system spatial-bandwidth product and simultaneously retrieving the unknown phase of a complex object (Zheng, 2016, 2014; Guo et al., 2016; Konda et al., 2020; Manuel Guizar-Sicairos and Fienup, 2008). It has potential applications such as digital pathology, in-vitro studies, automatic diagnosis, 3D imaging of thick samples and surface inspection (Konda et al., 2020). In this imaging modality, an object is illuminated by a coherent or partially coherent light source and a series of low-resolution intensity images are acquired by a digital camera equipped with low numerical aperture (NA) front optics. The highest spatial frequency that reaches the detector plane is defined by the cut-off frequency of the Coherent Transfer Function (CTF) of optical components. The digital sensor spatially samples the intensity information and its Nyquist sampling frequency defines the maximum un-aliased spatial frequency that can be faithfully represented in the captured image (Zheng, 2016; Goodman, 2017). By illuminating the object from different angles, the corresponding spatial frequency is shifted in the Fourier plane and thus, different sub-parts of this spectrum get passed through the CTF of the objective lens and reach the detector plane, where only the

light intensity is recorded while the electric field phase information is lost. Mathematically, recreating this process in the software and using these different sub-spectra together along with iteratively propagating the electric field back and forth between the sensor plane and the Fourier plane while using the recorded information of the absolute electric field, the complex extended Fourier spectrum is restored, which is equivalent to recovering the complex object transfer function with higher final spatial resolution. Over the years, many improvements have been proposed to the basic FPM algorithm, such as adaptive system correction (Bian et al., 2013), high numerical aperture implementation (Ou et al., 2015), complex pupil recovery (Ou et al., 2014; Manuel Guizar-Sicairos and Fienup, 2008), multilayer recovery (Tian and Waller, 2015), denoising methods (Zhang et al., 2017), Fresnel integral based wave propagation (Konda, 2017; Pan et al., 2019), to name a few.

In this work, we show how to use the Fresnel wave propagation integral to propagate the wave field from the object plane to the lens plane and the sensor plane while calculating the necessary wave field shift for off-axis LED illumination. In addition, the quadratic phase of the wave emanating from the LEDs is taken into account while previous works assume a plane wave illumination. Due to an
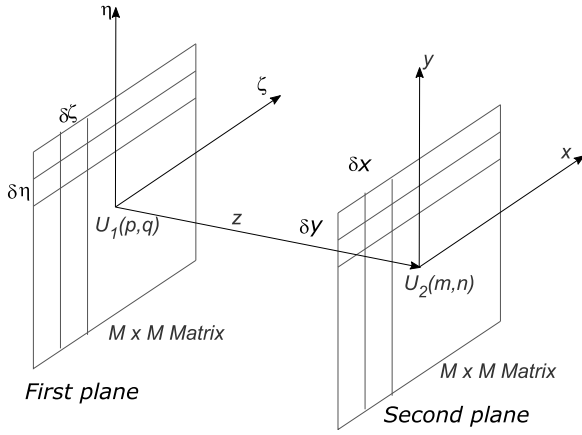

Fig. 1. Geometry for propagation of complex field between two planes by the Fresnel propagation.

accurate wave field propagation, this scheme can simulate the mixed bright/dark field images for a wide image patch where some parts of the object produce bright field image while other parts produce dark field image. It has been shown that such mixed bright/dark field images are important for low frequency phase information (Sun et al., 2018). By matching the boundary of the mixed bright/dark field captured image with the simulated image, we show how the LED misalignment with respect to their ideal position, such as lateral displacement and rotation can be estimated and corrected for. In addition, we show how to correctly recover off-center patches for wide field-of-view FP imaging by correcting for the objective lens distortion. The paper is organized as follows: Fresnel wave propagation integral using single Fourier Transform method is explained, FP recovery scheme is derived, and field calculation for off-axis illumination and off-axis image patch is explained. Recoveries from experimental images for USAF resolution target and a complex cartilage bone sample are shown for on-axis and off-axis image patches for a wide imaging area. Finally, the key points of the work are discussed and summarized.

2. Fresnel propagation integral: Single Fourier Transform method

The scalar wave propagation between two planes is described by the Fresnel propagation integral (Goodman, 2017):

$$U_2(x, y) = \frac{e^{ikz}}{i\lambda z} \exp\left(i\frac{k}{2z}(x^2 + y^2)\right) \cdot$$
$$\iint_{-\infty}^{+\infty} U_1(\zeta, \eta) \exp\left(i\frac{k}{2z}(\zeta^2 + \eta^2)\right) \cdot$$
$$\exp\left(-i\frac{k}{z}(x\zeta + y\eta)\right) d\zeta d\eta \qquad (1)$$
$$= \frac{e^{ikz}}{i\lambda z} \exp\left(i\frac{k}{2z}(x^2 + y^2)\right) \mathcal{F}\left\{U_1(\zeta, \eta) \exp\left(i\frac{k}{2z}(\zeta^2 + \eta^2)\right)\right\}$$
$$, \text{ at } f_x = x/(\lambda z), f_y = y/(\lambda z) \qquad (2)$$

where $U_1(\zeta, \eta), U_2(x, y)$ are the electric fields at the first and the second planes respectively, z is the separation distance between the planes, $k = 2\pi/\lambda$, $\mathcal{F}\{\cdot\}$ is the Fourier Transform operator. This scheme is called the Single Fourier Transform approach. This equation can be digitally calculated by discretizing the input and the output fields as shown in Fig. 1: $\delta\zeta$, $\delta\eta$ are sampling distances on the input plane, δx, δy are the sampling distances on the second plane, $x_m = m\delta x$, $y_n = n\delta y$, $\zeta_p = p\delta\zeta$, $\eta_q = q\delta\eta$, $U_1(p, q) \equiv U_1(p\delta\zeta, q\delta\eta)$, $U_2(m, n) \equiv U_2(m\delta x, n\delta y)$, where m, n, p, q are matrix indices with the bounds: $-M/2 \leq m \leq M/2 - 1$, $-N/2 \leq n \leq N/2 - 1$, $-P/2 \leq p \leq P/2 - 1$, $-Q/2 \leq q \leq Q/2 - 1$.

$M \times N$. $P \times Q$ are the two-dimensional matrix sizes. The discretized version of Eq. (1) reads

$$U_2(m\delta x, n\delta y) = \frac{e^{ikz}}{i\lambda z} \exp\left(i\frac{k}{2z}\left((m\delta x)^2 + (n\delta y)^2\right)\right) \cdot$$
$$\sum_p \sum_q \left\{ U_1(p\delta\zeta, q\delta\eta) \exp\left(i\frac{k}{2z}\left((p\delta\zeta)^2 + (q\delta\eta)^2\right)\right) \cdot$$
$$\exp\left(-i\frac{k}{z}(m\delta x p\delta\zeta + n\delta y q\delta\eta)\right)\right\} \delta\zeta\delta\eta \qquad (3)$$

For the case of same sized matrices on the input and the output planes, $M = P$, $N = Q$, the above equation can be calculated as:

$$U_2(m, n) = \frac{e^{ikz}}{i\lambda z} \exp\left(i\frac{k}{2z}\left(x_m^2 + y_n^2\right)\right) \cdot$$
$$\text{FFT}\left\{ U_1(p, q) \exp\left(i\frac{k}{2z}\left(\zeta_p^2 + \eta_q^2\right)\right)\right\} \qquad (4)$$

where FFT$\{\cdot\}$ is the digital Fast Fourier Transform operation. In this implementation, there is a fixed relationship between the sampling distances on the two planes. Given by:

$$\delta x = \lambda z/(M\delta\zeta), \ \delta y = \lambda z/(N\delta\eta) \qquad (5)$$

In the single FT Fresnel propagation, the physical size of the output plane can be either bigger, smaller or of equal size as the physical size of the input plane, and this is dictated by the relationship in Eq. (5).

3. FPM recovery based on Fresnel propagation

In a single thin-lens imaging model of the whole setup as shown in Fig. 2, the scalar electric field at the detector plane can be written as (Goodman, 2017):

$$U_4(u, v) = \exp\left(i\frac{k}{2z_2}(u^2 + v^2)\right) \mathcal{F}\left\{ P(x, y) \exp(ikW(x, y)) \cdot$$
$$\mathcal{F}\left(U_1(\zeta, \eta) \exp\left(i\frac{k}{2z_1}(\zeta^2 + \eta^2)\right)\right)\right\} \qquad (6)$$

where $P(x, y)$ is the pupil amplitude function and $W(x, y)$ is the wavefront error. This is the linear–shift-variant model of imaging, which is able to better represent the wave propagation from the object plane to the detector plane over a wider patch (Pan et al., 2019; Konda, 2017). Often the exponential phase factor on the object plane coordinates ζ, η in the expression is ignored and one gets a linear–shift-invariant Fraunhofer imaging model (Goodman, 2017).

$$U_4(u, v) = h(u, v) \otimes u_g(u, v) = \mathcal{F}^{-1}\left\{\mathcal{F}\{(h(u, v))\} \cdot \mathcal{F}\{(u_g(u, v))\}\right\}$$
$$= \mathcal{F}^{-1}\left\{CTF(f_u, f_v) \cdot U_g(f_u, f_v)\right\} \qquad (7)$$

where $h(u, v)$ is the coherent point-spread-function, $CTF(f_x, f_y)$ is the coherent transfer function, $u_g(x, y) = U_1(x/K, y/K)$ is the magnified geometrical image of the $U_1(\zeta, \eta)$ and the magnification is $K = -z_2/z_1$. Most of the published work on FP is based on the Fraunhofer imaging model (Zheng, 2016) and it will not be further discussed here. Instead, we will focus on the derivation of the FP recovery (forward and backward model) for the Fresnel propagation, first published by Konda et al. see Konda (2017). The discretized field at the left side of the lens is (ignoring the constant factors such as $e^{ikz}/(i\lambda z)$ in all subsequent calculations):

$$U_2(m, n) = \exp\left(i\frac{k}{2z_1}(x_m^2 + y_n^2)\right) \text{FFT}\left\{ U_1(p, q) \exp\left(i\frac{k}{2z_1}(\zeta_p^2 + \eta_q^2)\right)\right\}$$
$$= \exp\left(i\frac{k}{2z_1}(x_m^2 + y_n^2)\right) \cdot Fact_1 \qquad (8)$$

where the factor $Fact_1$ is implicitly defined. $U_1(p, q)$ is the discretized field after the object, which can be written for a uniform spherical wave illumination as

$$U_1(p, q) = O(p, q) \cdot \exp\left(i(k_\zeta \zeta_p + k_\eta \eta_q)\right) \cdot \exp\left(i\frac{k}{2L}(\zeta_p^2 + \eta_q^2)\right) \qquad (9)$$
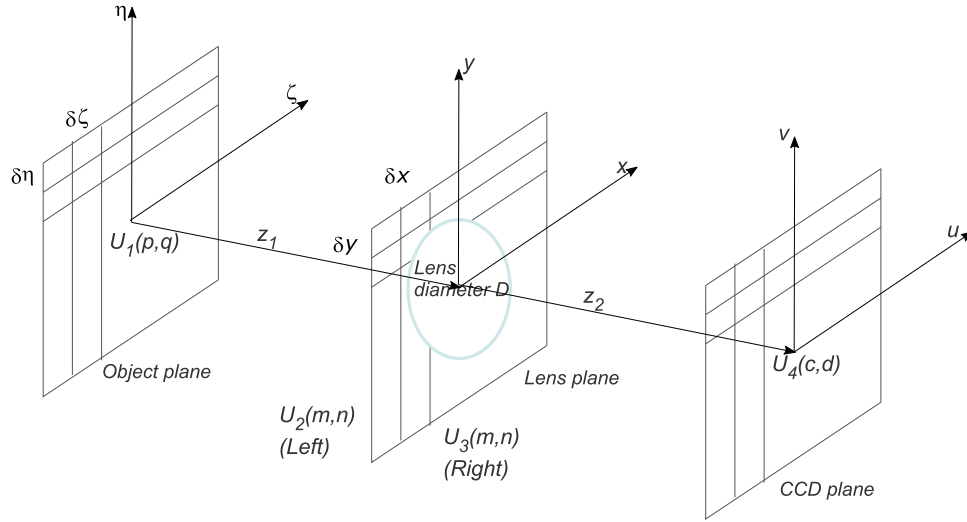
Fig. 2. Fresnel propagation imaging model, object plane, lens plane and image plane.

$O(p,q)$ is the complex object transmittance function, L is the LED plane to sample plane distance, and k_ζ, k_η are the illuminating wave component vectors. The second exponential factor takes into account the spherical wavefront (approximated as parabolic) from the LED falling on the sample plane. For perpendicular illumination, $k_\zeta = k_\eta = 0$ and the diffracted field U_2 will have zero-frequency at the center of the lens (at the $M/2+1, N/2+1$ location in the $U_2(m,n)$ matrix). For oblique illumination, the diffracted field U_2 will have its zero-frequency shifted laterally in the lens plane. It will be shown later how to calculate this shifted center. The lens transfer function LTF is:

$$\text{LTF}(m,n) = P(m,n)\exp(-ikW(m,n))\exp\left(-\frac{ik}{2f}(x_m^2+y_n^2)\right)$$
$$= \mathcal{P}(m,n)\exp\left(-\frac{ik}{2f}(x_m^2+y_n^2)\right) \quad (10)$$

where $\mathcal{P}(m,n)$ is the complex pupil function. The field immediately after the lens, with $W(m,n)$ modeling the discretized lens wavefront aberrations, is given by :

$$U_3(m,n) = P(m,n)\exp(-ikW(m,n))\exp\left(-\frac{ik}{2f}(x_m^2+y_n^2)\right)\cdot$$
$$\exp\left(i\frac{k}{2z_1}(x_m^2+y_n^2)\right)\cdot Fact_1 \quad (11)$$

The field at the image plane is:

$$U_4(c,d) = \exp\left(i\frac{k}{2z_2}(u_c^2+v_d^2)\right)\text{FFT}\left\{U_3(m,n)\exp\left(i\frac{k}{2z_2}(x_m^2+y_n^2)\right)\right\}$$
$$= \exp\left(i\frac{k}{2z_2}(u_c^2+v_d^2)\right)\text{FFT}\left\{P(m,n)\exp(-ikW(m,n))\cdot\right.$$
$$\left[\exp\left(\frac{-ik}{2f}(x_m^2+y_n^2)\right)\exp\left(i\frac{k}{2z_2}(x_m^2+y_n^2)\right)\cdot\right.$$
$$\left.\left.\exp\left(i\frac{k}{2z_1}(x_m^2+y_n^2)\right)\right]\cdot Fact_1\right\} \quad (12)$$

The factor in the square brackets [·] is '1' based on the thin lens equation of geometrical optics. Thus we get:

$$U_4(c,d) = \exp\left(i\frac{k}{2z_2}(u_c^2+v_d^2)\right)\cdot$$
$$\text{FFT}\left\{P(m,n)\exp(-ikW(m,n))\cdot Fact_1\right\} \quad (13)$$

This is the forward imaging model (Konda, 2017). The update step is performed on the propagated field U_4, that is, the amplitude of U_4 is
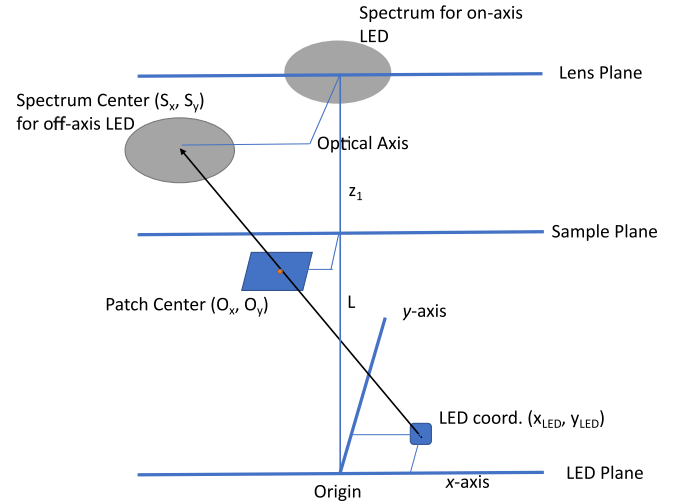

Fig. 3. Shift of the diffracted field on the lens plane for off-axis LED illumination (Konda, 2017).

replaced by the amplitude of the image captured by the camera while the phase of U_4 is kept as is,

$$U_{4,upd} = \sqrt{I}\arg(U_4) \quad (14)$$

The updated field $U_{4,upd}$ is propagated back to the left side of the lens plane (Fig. 2) and we get:

$$U_{3,upd}(m,n) = \exp\left(-i\frac{k}{2z_2}(u_c^2+v_d^2)\right)\text{IFFT}\left\{U_{4,upd}(c,d)\right\} \quad (15)$$

Note that the exponential phase factors before the FFT in Eqs. (13) and (15) cancel each other, so they do not have to be calculated in the first place. The sub-part of the field matrix at the left of the lens plane which belongs to the oblique illuminated plane wave, and the complex pupil function can be updated based on the Newton gradient descent like algorithms (Zheng, 2016; Tian and Waller, 2015; Manuel Guizar-Sicairos and Fienup, 2008). That is:

$$U_{2,upd} = U_2 + \frac{|\mathcal{P}|\,\mathcal{P}^*(U_{3,upd}-U_2)}{|\mathcal{P}|_{max}(|\mathcal{P}|^2+\delta_1)} \quad (16)$$

$$\mathcal{P}_{upd} = \mathcal{P} + \frac{|U_2|\,U_2^*(U_{3,upd}-U_2)}{|U_2|_{max}(|U_2|^2+\delta_2)} \quad (17)$$
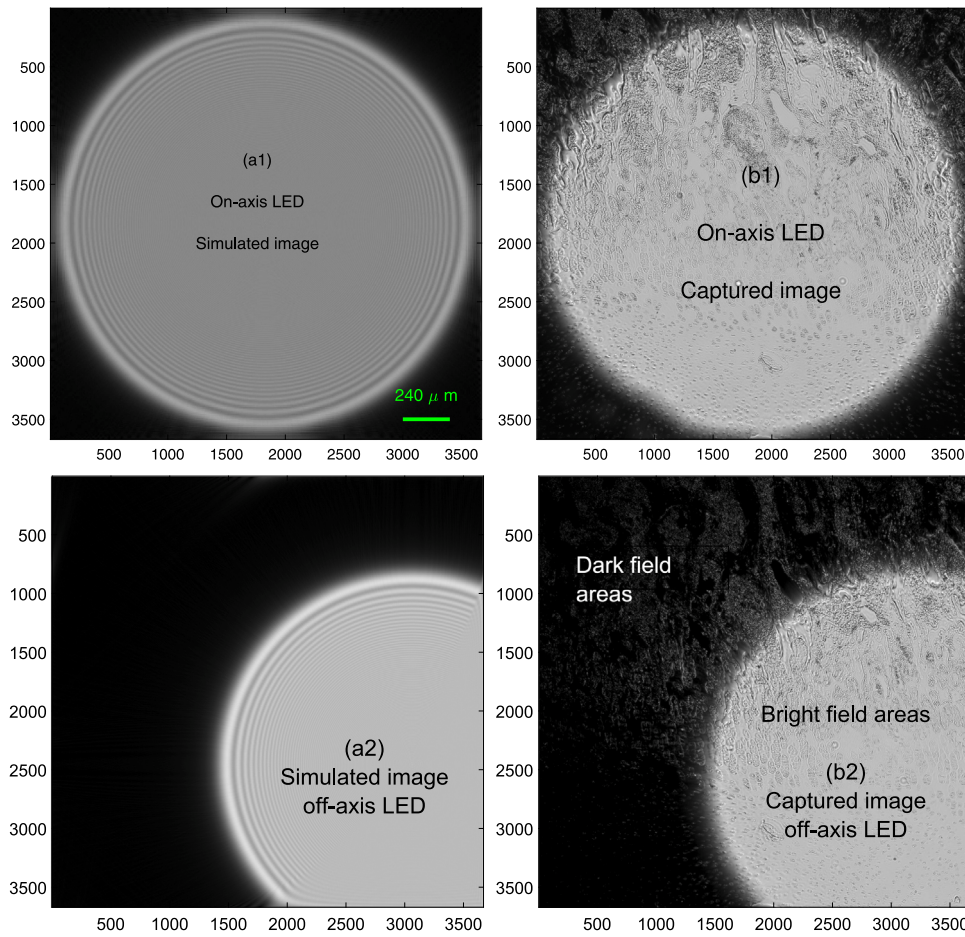
Fig. 4. Calibration of parameters, central image patch, matching forward propagated images bright/dark field boundary (a1, a2) with the captured images (b1, b2). Note a good match of the bright/dark field boundary between the captured and numerically propagated forward images.

where δ_1, δ_2 are small numbers to avoid division by zero. When the field matrix at the lens plane has been updated for all the captured images and the required convergence has been achieved after a number of iterations between the lens plane and the detector plane, the high resolution object can be reconstructed by finally propagating $U_{2,upd}$ back to the object plane as follows:

$$O(p,q) = \exp\left(-i\frac{k}{2L}(\zeta_p^2 + \eta_q^2)\right) \exp\left(-i\frac{k}{2z_1}(\zeta_p^2 + \eta_q^2)\right) \cdot$$
$$\text{IFFT}\left\{U_{2,upd}(m,n)\right\} \tag{18}$$

The Fresnel based FP algorithm is given in the Appendix as a pseudo-MATLAB code.

3.1. Field calculation for oblique illumination and for off-center image patch

As shown in Fig. 3, the shift of the center of the diffracted field at the lens plane for off-axis illumination can be calculated as (Konda, 2017)

$$s_x = \frac{z_1(x_{LED} - o_x)/L - o_x}{\delta x} \tag{19}$$

$$s_y = \frac{z_1(y_{LED} - o_y)/L - o_y}{\delta y} \tag{20}$$

where o_x, o_y are the center of the object patch chosen for recovery. The shifts s_x, s_y are in terms of number of pixels in the matrix $U_{2,upd}$

from their zero-frequency location $(M/2+1, N/2+1)$ for perpendicular illumination. For ease of programming, the $U_{2,upd}$ matrix is not shifted as such, rather the complex pupil function matrix $\mathcal{P}$ is multiplied by the sub-part of $U_{2,upd}$ matrix at the appropriately shifted center to select the part of the spectrum that gets passed on to the detector plane.

4. Recovery from experimental images

The following hardware was used for acquiring experimental images. A Basler camera (Model acA5472-17um, pixel size 2.4 μm × 2.4 μm, 12 bit resolution, full-frame pixels 5496 × 3672, sensor size 13.19 mm × 8.81 mm). A 15 × 15 LED board with LED spacing 4.0 mm, central wavelength 0.52 μm. A finite-conjugate objective with $NA = 0.08$, magnification was either 2X or 4X as mentioned later (by employing different extension tube lengths). Note that this setup gives a rather wide field of view, measuring 3297 μm × 2203 μm for the 4X magnification and 6595 μm × 4405 μm for the 2X magnification. It should be noted that the objective is not designed for such a big sensor and hence, there will be severe vignetting for off-axis viewing patches outside the designed FoV of these objectives, especially for the 2X magnification setup. For the mathematical modeling, we exploit the well-known fact that any optical train of multiple co-axial lenses can be modeled as a generalized system featuring an effective focal length, an entrance pupil and an exit pupil, a distance z_o from the object to the entrance pupil, and a distance z_i from the exit pupil to the image plane (Goodman, 2017). While derived for a single thin lens in chaps. 2 and 3, the z_o and z_i distances and the aperture stop diameter D used

Captured images   Calculated images, no correction   Calculated images with correction
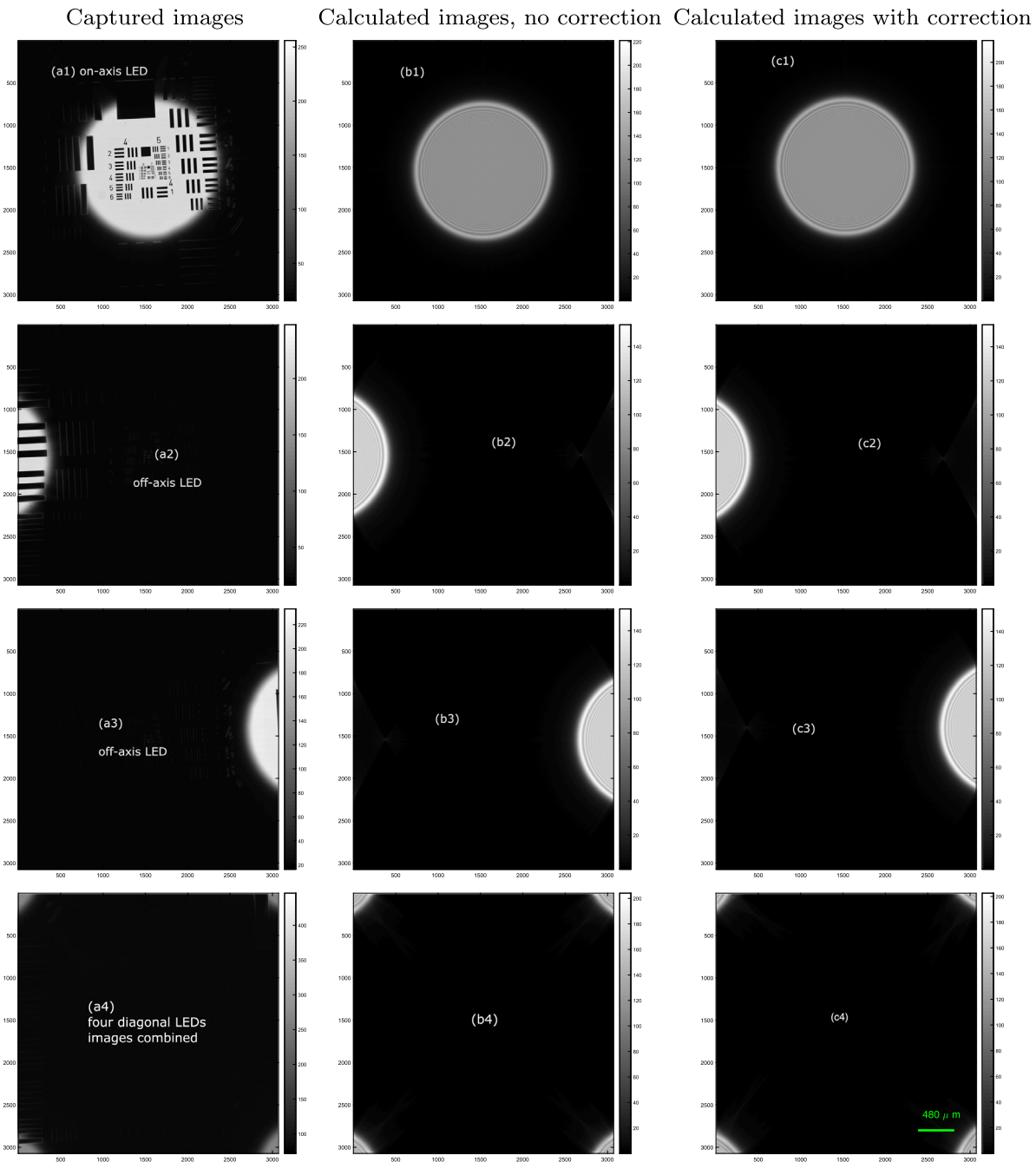

Fig. 5. Calibration of LED board decenter and rotation, central wide patch 3072 × 3072 pixels, 2X magnification, Captured images(a1, a2, a3, a4), Forward images with no LED displacement having poor match of bright/dark field boundary with the captured images (b1, b2, b3, b4), Forward images with estimated LED displacement and rotation with good match of bright/dark field boundary with the captured images (c1, c2, c3, c4). Note a good match of the bright/dark field boundary between the captured and numerically propagated forward images after calibration (for example, images a3 and c3, a4 and c4).

in the remainder of this article refer to such a generalized model for the objective lens setup.

4.1. Calibration of distance z_1 and pupil diameter D

The distance between the object plane and the entrance pupil of lens z_1 and the lens entrance pupil diameter D are only known approximately based on the given objective focal length, magnification and numerical aperture. Since the Fresnel model calculates the field at the lens plane, it can simulate the clipping of the field by the objective lens finite aperture stop diameter D. It can correctly simulate

mixed bright/dark field images for very wide patches, which cannot be correctly simulated by the Fraunhofer imaging model (Pan et al., 2019; Konda, 2017). We calculate the parameters z_1 from the lens equation and the known magnification. Then we adjust D until the forward propagated images match with the recorded mixed bright/dark field images for on-axis and off-axis LEDs. One such simulation is shown in Fig. 4, where the clipping of the forward propagated bright image is matched to the captured image. We show here just two sets of images but all of them match after calibration. Note that this procedure can be automated using optimization algorithms by matching the forward
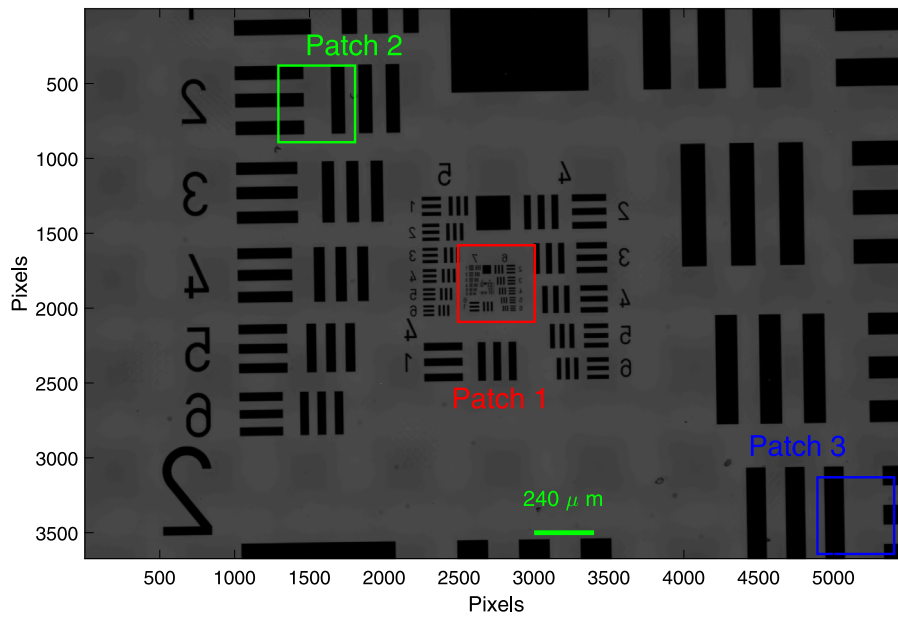
Fig. 6. USAF resolution target, low resolution incoherently combined image, 5496 × 3672 pixels full sensor, 4X magnification, physical image size on the sample plane was 3297 μm × 2203 μm. This image was obtained by incoherently adding individual intensity images from all the LEDs.
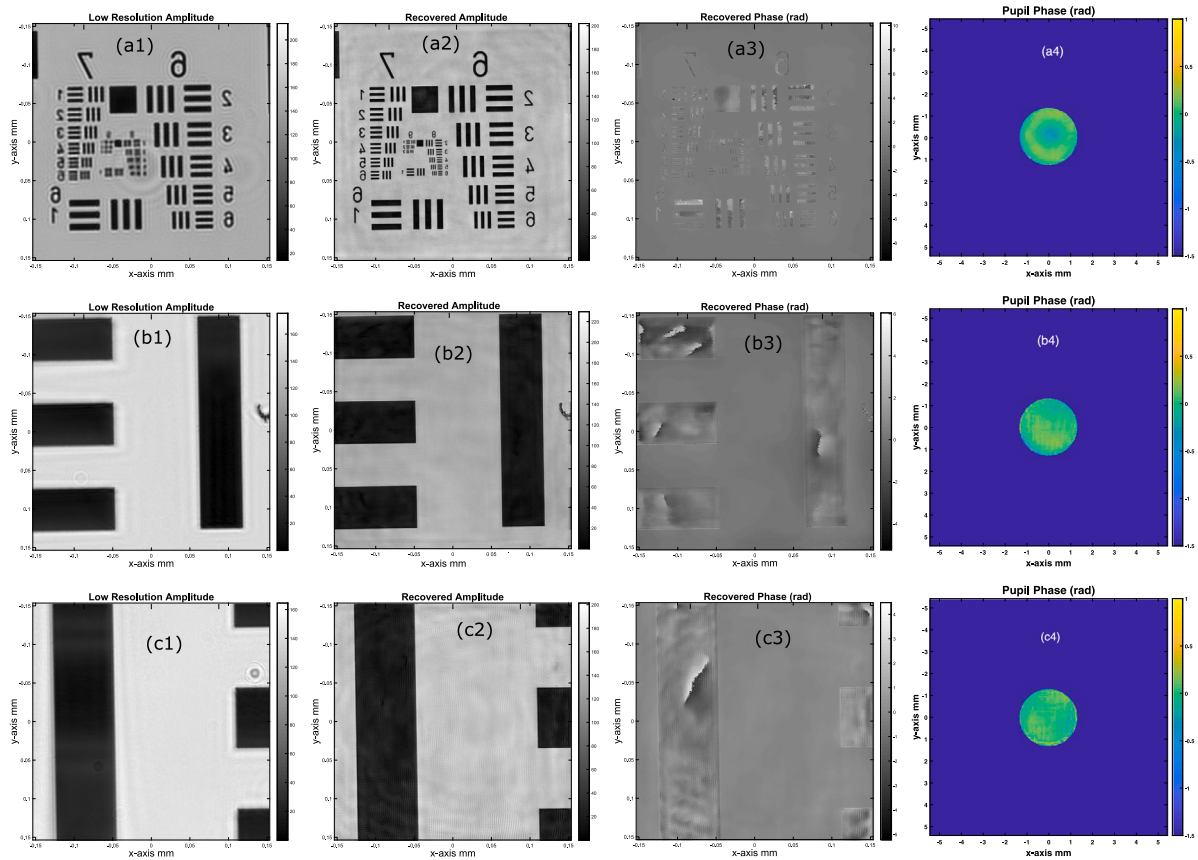

Fig. 7. USAF resolution target recovery, patch size 512 × 512 pixels, 4X magnification, (a1–a4), patches from Fig. 6, patch 1, (b1–b4), patch 2, (c1–c4), patch 3. The quality of the phase reconstruction should be judged by the uniformity of the gray-tone background, as the phase is allowed to assume any value in the opaque regions.

image Bright/dark ring with the captured image and using image processing schemes, such as the structural similarity metric (SSIM) (Wang et al., 2004) to get the best calibrated values for s_x, s_y which give the highest similarity between the experimental and modeled images.

However, for simplicity, we opted for manual adjustment by overlaying the two images on top of each other to estimate the best match visually. In this example, the calculated distance z_1 was 12.5 mm and the aperture stop diameter D 2.4 mm.
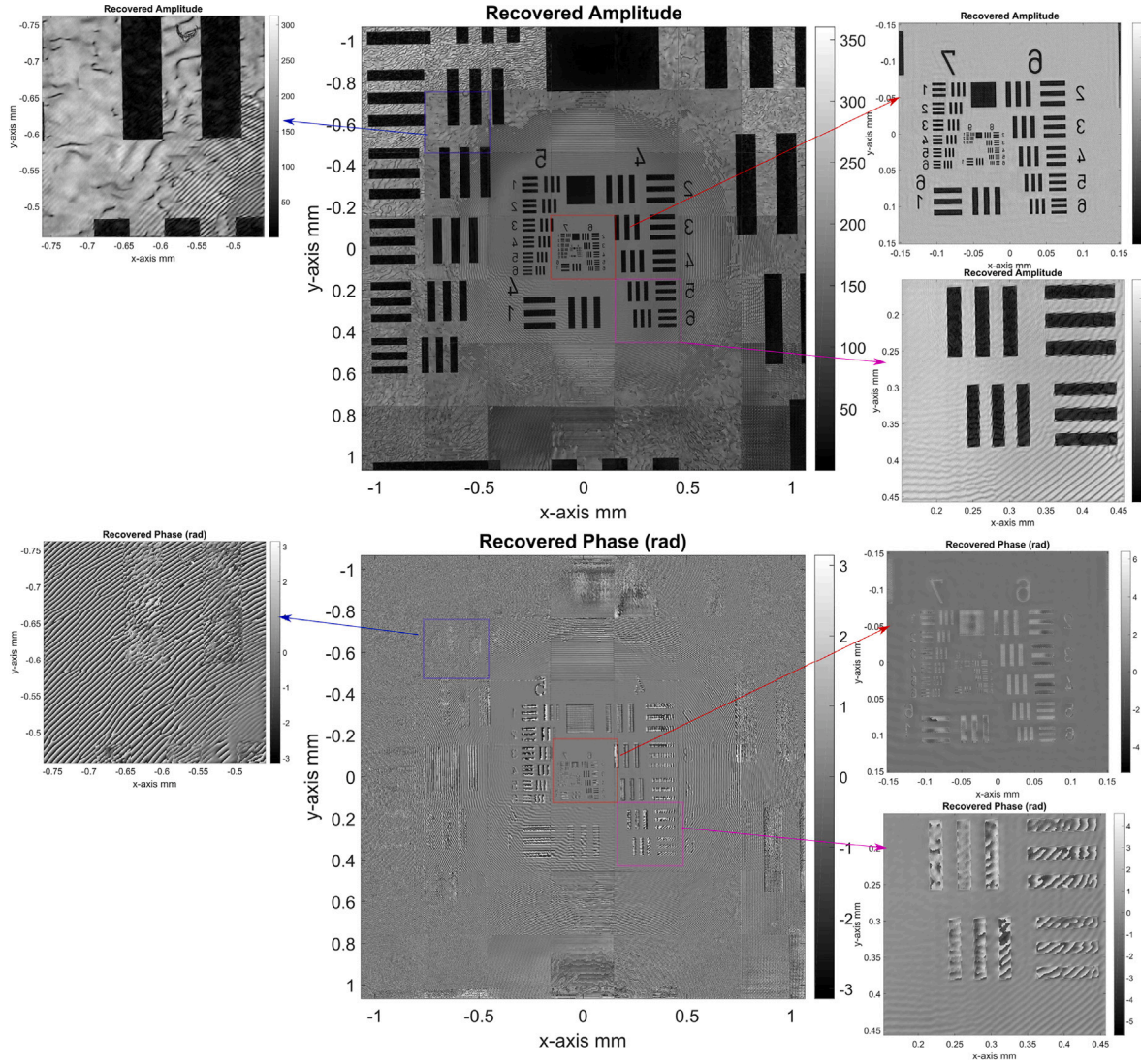
Fig. 8. USAF resolution target, wide field recovery using the traditional Fraunhofer model, 4X magnification, 512 × 512 pixels (307 μm × 307 μm) area each sub-patch, total 3584 × 3584 pixels. Note severe artifacts and wrinkles for off-axis patches.

4.2. Calibration of LED-board position misalignment and rotation

A rigid body model for misalignment of the LED board is used (Sun et al., 2016) here. The LED position is given by:

$$x_{LED}(m, n) = LED_{gap} \cdot (\cos(\theta)m + \sin(\theta)n) + dx \qquad (21)$$

$$y_{LED}(m, n) = LED_{gap} \cdot (-\sin(\theta)m + \cos(\theta)n) + dy \qquad (22)$$

where m, n is the LED index, dx, dy is the unwanted displacement of the central LED from the optical axis, θ is the unwanted rotation of the LED matrix with respect to the x-axis and LED_{gap} is the spacing between adjacent LEDs (Sun et al., 2016). By matching the bright/dark field boundary of captured image of a wide patch corresponding to the central LED with the simulated forward image, one can extract the displacement parameters dx and dy. An example is given in Fig. 5 where the extracted LED displacement was $dx = -0.1$ mm and $dy = -0.4$ mm. Similarly, by matching the bright/dark field boundary of captured images with the simulated images for off-axis LEDs, one can extract the LED matrix rotation error. In this test example, we extracted the θ parameter to be 2.65^0 degree. Note that this is a direct procedure which is implemented before the FPM recovery, while in other works (Zhou et al., 2018; Sun et al., 2016; Pan et al., 2017; Liu et al., 2017; Eckert et al., 2018), the LED position correction is

usually done within the FPM recovery algorithm using an additional optimization loop.

4.3. Recovery: USAF 1951 resolution target, 4X magnification

4.3.1. Fresnel model FPM recovery

Full-frame images were captured using the 15 × 15 LED matrix. The incoherently combined low resolution full-frame image of the resolution target is shown in Fig. 6.

Patches of 512 × 512 pixels were recovered for different areas on the full-frame images with an up-scaling factor of 6 (giving high resolution matrix size of 3072 × 3072) and $NA_{synth} = 0.44$ was recovered. The LED to sample distance was 113 mm. The objective magnification was 4X. The LED board was carefully placed so there was no misplacement or rotation of the LED board. The results of the recovery are given in Fig. 7, and it can be seen that the quality of the object recovery (amplitude and phase) as well as the pupil are excellent up to the corner of the FoV using the offset calibration procedure as explained. The three-bar pattern of Group 9 Element 3 can be easily resolved in the central patch. Note that far away from the central area of the USAF target, there are no fine features in the resolution target and hence it is difficult to quantify the recovered resolution for off-axis patches.
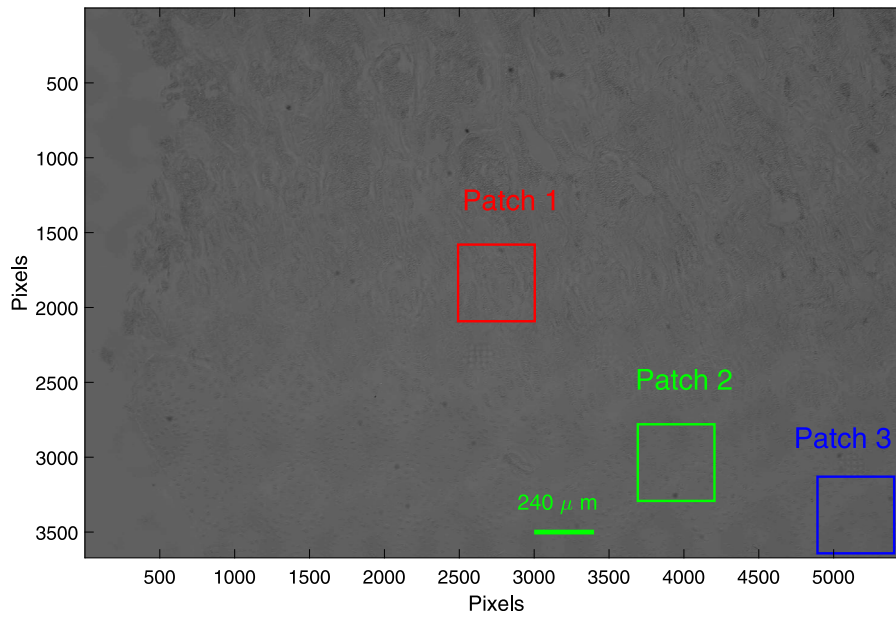
Fig. 9. Bone cartilage sample, low resolution incoherently combined image, 5496 × 3672 pixels full sensor, 4X magnification, physical image size on the sample plane is 3297 μm × 2203 μm.
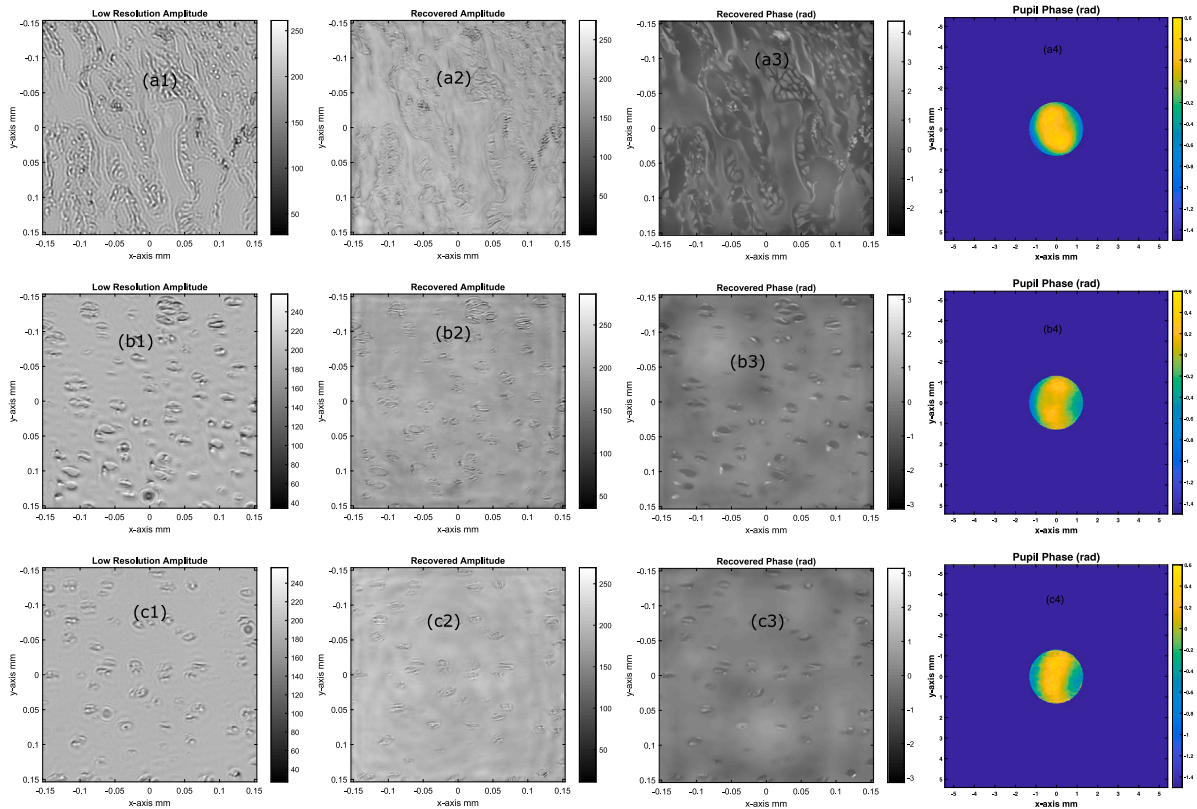

Fig. 10. Cartilage Bone Sample recovery, patch size 512 × 512 pixels, 4X magnification, patches from Fig. 9, (a1–a4), patch 1, (b1–b4), patch 2, (c1–c4), patch 3.

4.3.2. Fraunhofer model FPM recovery

For the sake of comparison, 7 × 7 segments, each of size 512 × 512 pixel, were recovered using the traditional Fraunhofer model. In this case, the *k*-vector *x*- and *y*- components of the incoming uniform plane for off-axis LED and off-axis image patch are calculated as follows (Zheng, 2016; Konda, 2017) (see Fig. 3):

$$k_x = k(o_x - x_{LED}) / \sqrt{(o_x - x_{LED})^2 + (o_y - y_{LED})^2 + L^2}$$

$$k_y = k(o_y - y_{LED}) / \sqrt{(o_x - x_{LED})^2 + (o_y - y_{LED})^2 + L^2} \qquad (23)$$

The calculated k_x and k_y values are used to select the sub-spectrum of the object spectrum at the Fourier plane to be passed on to the sensor plane (Zheng, 2016). The results of the FPM recovery are given in Fig. 8 by combining all the segments in one picture. The central patches are recovered successfully with good amplitude and phase. It can be seen that for off-axis image patches, there are a lot of artifacts in the recovered amplitude and phase, and these artifacts get worse
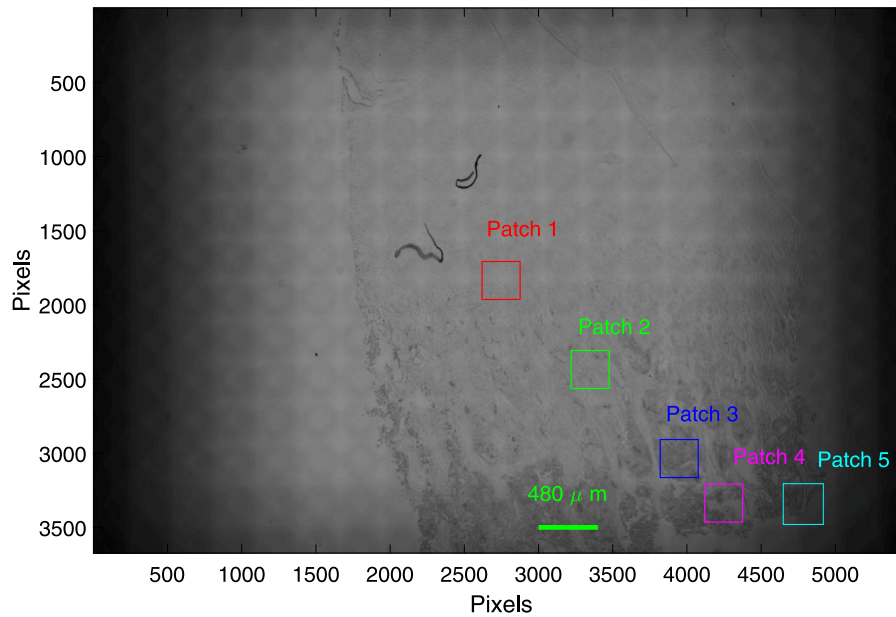
Fig. 11. Bone cartilage incoherently combined low resolution image, 5496 × 3672 pixels full senor, 2X magnification, physical image size on the sample plane is 6595 μm × 4405 μm.

towards the corner areas. This poor performance at high angles is essentially caused by the limitations of the Fraunhofer model for image formation as well as by uncorrected distortion of the objective lens. The Fraunhofer model is valid for a small patch as it ignores the source-plane complex exponential phase factor $\exp(ik/(\zeta^2 + \eta^2)/(2z))$ of Eq. (1). In addition, the parabolic factor $\exp\left(-i\frac{k}{2L}(\zeta_p^2 + \eta_q^2)\right)$ of Eq. (9) is not taken into account for wide FoV imaging, hence yielding ripples and jumps in the recovered amplitude and phase.

4.4. Recovery: Cartilage bone sample, 4X magnification

4.4.1. Fresnel model FPM recovery
An unstained histological section of thickness approximately 4.0 μm was obtained near the ossification front of the femoral epiphysis of a Landrace piglet, [Mürer et al.] for further details. This is a complex target with both amplitude and phase variations across the sample. The same 4X setup was used as in the previous example. The low-resolution incoherently combined full-frame image is shown in Fig. 9. The results of the recovery of different patches are given in Fig. 10, and it can be seen that the quality of object recovery (amplitude and phase) as well as the pupil are excellent up to the corner of the FoV. We also performed Fraunhofer model based recovery and the results were similar to those in Fig. 8 with increasing artifacts and ripples in the recovered amplitude and phase towards the edge of the FoV.

4.5. Extreme wide FoV recovery: Cartilage bone sample, 2X magnification

We used 2X magnification configuration with the same Basler camera and LED board to capture images and recover the cartilage bone sample. This was done to explore the case of an extremely wide FoV of size 6595 μm × 4405 μm on the sample plane. The full-frame incoherently combined image from all the LED images is shown in Fig. 11 and it can be seen that the edges of the image are very dark.

This is due to excessive pupil vignetting for the extreme FoV areas. The LED plane to the sample plane distance was 160.0 mm. The results of the recovery (low resolution 256 × 256 matrix size) are given in Figs. 12 and 13, and it can be seen that the quality of the object recovery (amplitude and phase) as well as the pupil are excellent up to a center offset of $o_x = o_y = 1.8$ mm (patch 4), but not beyond.

Since this is a 2X magnification, the FoV is twice as large compared to the 4X magnification. The lens objective is not designed for such a wide sensor and there is excessive pupil vignetting for far off-axis patches. The pupil vignetting effect is clearly visible in the recovered pupil amplitude in Fig. 13 and with increased FoV, it gets worst. The recovery is poor for patch center offset greater than patch 4 since many of the recorded images suffer from excessive pupil vignetting. An additional feature to be noted is that for the on-axis patch, the recovered spectrum is symmetrical about the zero spatial frequency, but for off-axis patches, the recovered spectrum is not symmetrical. One side of the spectrum is recovered up to a higher spatial frequency as compared to the other side, since the LEDs angles are not symmetrical about the zero-th diffraction order for an off-axis patch. This could also be another reason that the image recovery is not successful for extreme off-axis patches as shown in Fig. 13. These results show that there is a certain maximum limit of the FoV that can be successfully recovered with a given objective lens. Note that for the 4X configuration as shown in Fig. 10, we were able to successfully recover up to the corner of the FoV since the pupil vignetting was negligible.

5. Discussions

Many interesting features of the Fresnel based propagation and FPM recovery can be highlighted. The main feature is the inclusion of the source complex exponential phase factor: $\exp(ik/(\zeta^2 + \eta^2)/(2z))$ in the calculation (Eq. (1) and subsequent equations) which makes the propagation linear–shift-variant and hence it can better represent the propagated field over a wider patch. In the traditional Fraunhofer FP imaging model, this phase factor is ignored and hence the imaging model becomes inaccurate for wide imaging patches. We have also included the complex exponential factor $\exp\left(-i\frac{k}{2L}(\zeta_p^2 + \eta_q^2)\right)$ that represents the spherical wave from the LED. Usually, this factor is ignored, but this factor could become important if the LED to sample plane distance is small. Another feature of the Fresnel scheme is that the exponential phase factors inside the square brackets in Eq. (12) cancel each other, thus making the sampling requirements more relaxed as these factors do not need to be calculated in the first place. Furthermore, the preceding exponential phase factors in Eqs. (13) and (15) also get canceled. Another feature is that the field is propagated to the lens

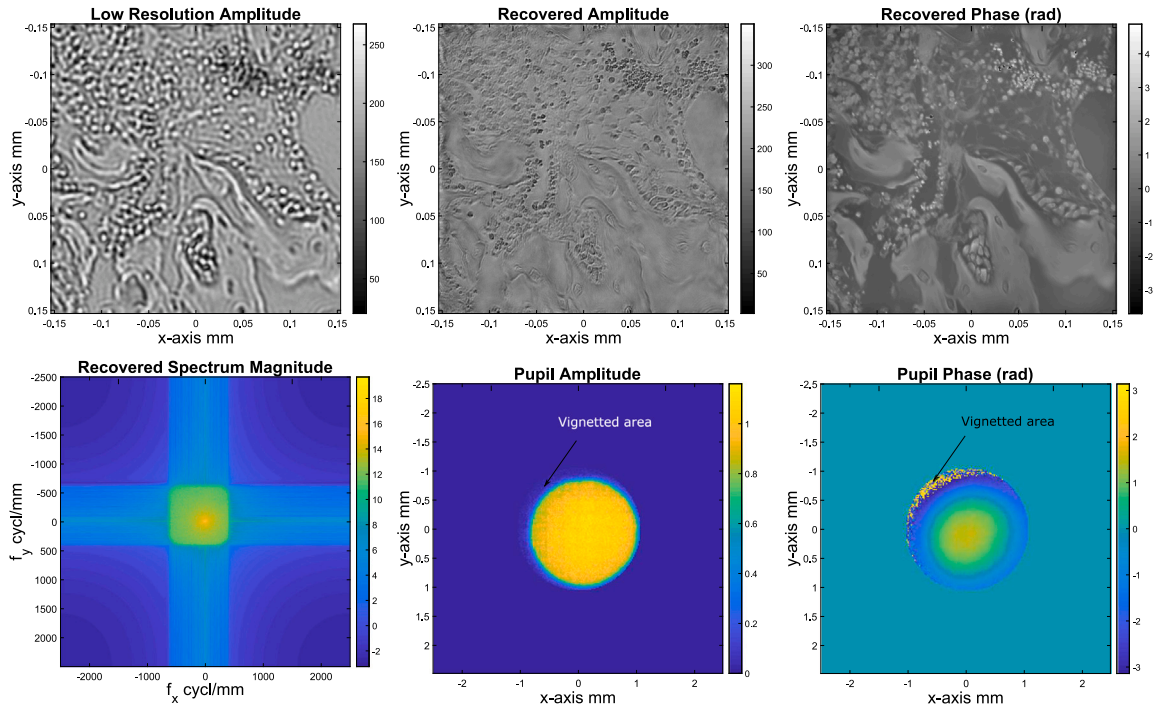## Patch 1 in figure 11
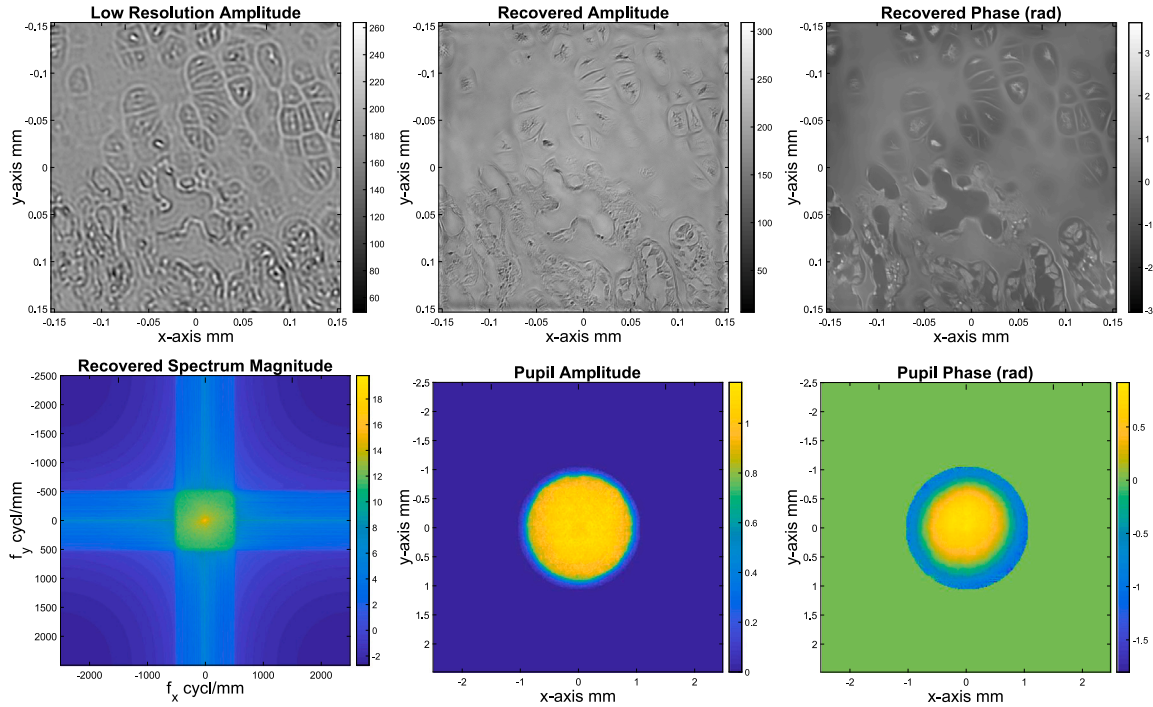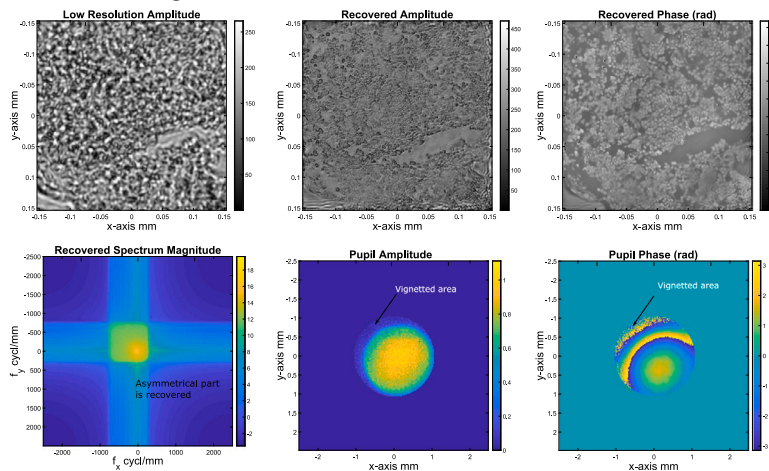

Patch 2 in figure 11

Fig. 12. Cartilage Bone Sample recovery, patch size 256 × 256 pixels, 2X magnification, off-axis patches, patch 1 and 2 in Fig. 11.

plane instead to the Fourier plane and hence, the clipping of the field by the lens finite aperture is correctly calculated. This is why the mixed bright/dark field images can be simulated by the Fresnel propagator while they cannot be calculated by the Fraunhofer imaging model. Note that there are many ways to implement the Fresnel propagation integral numerically (Goodman, 2017), for example by a triple Fourier transform approach or by a single Fourier transform. The single Fourier Transform approach makes it possible to have either expanding or

contracting size of the second plane while keeping the same overall matrix size. The size of the expanded or contracted second plane is determined by the fundamental relation given in Eq. (5). In the present work, we had to use the single Fourier transform approach since the object size is usually much smaller that the size of the field on the lens plane, and again, the detector plane size is smaller than the lens plane size. We have shown how the diffracted field at the lens plane shifts for off-axis LEDs and for off-center patch. However, this basic

Patch 3 in figure 11

Patch 4 in figure 11
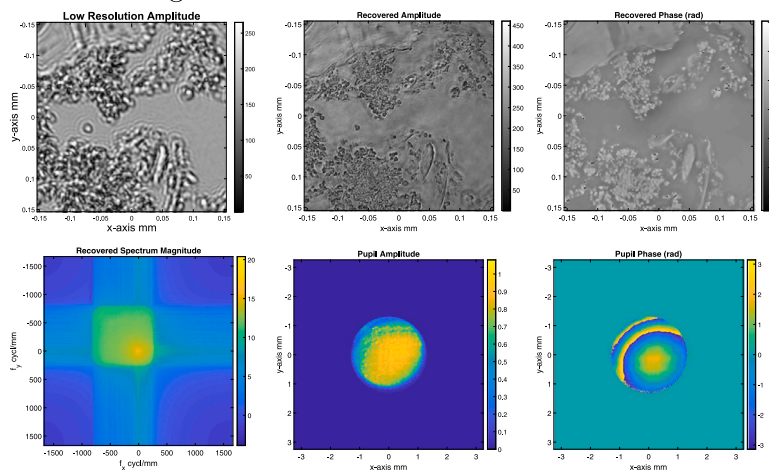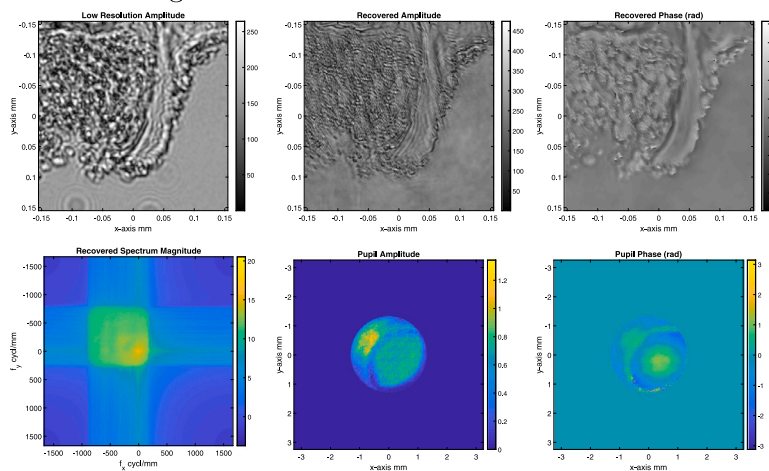

Patch 5 in figure 11

Fig. 13. Cartilage Bone Sample recovery, patch size 256 × 256 pixels, 2X magnification, off-axis patches, patch 3, 4 and 5 in Fig. 11. Patch 5 is not successfully recovered due to severe vignetting.

relation is not valid if there are LED misalignments or if the imaging lens has distortion which shifts the apparent center of the diffracted field. We have shown how to correct for the LED misalignment and lens distortion for the off-axis patch center and successfully recovered off-axis image patches up to the corner of the sensor for 4X magnification. For the extreme wide FoV case with 2X magnification objective, it

has been shown that due to excessive pupil vignetting, it is not possible to recover the patches beyond a certain offset from the optical axis. It can be recommended that for low magnification objectives to be used with a wide area sensor, an objective should be chosen which is designed to operate without pupil vignetting for such extreme FoV. The size of the image patch chosen for recovery should be smaller than

the coherence area of the LED propagated field falling on the sample plane as dictated by the Van-Cittert Zernike theorem for the coherent imaging model to be valid (Zheng, 2016). In the present work, we have not used any image pre-processing for simplicity, such as noise removal or LED intensity correction. If these pre-processing steps are included, the quality of the recovered images will be slightly better.

6. Summary and conclusions

We have derived an FPM recovery scheme based on the Fresnel propagation integral and developed a simple scheme to estimate and correct for the LED misalignment correction for off-center image patches. In addition, the quadratic phase of the wave emanating from the LEDs is taken into account. The advantage of using the Fresnel integral is that it calculates the wave propagation accurately for a wider image patch and that it can simulate mixed bright/dark field images in the same image patch. These features have been used for matching the numerically propagated forward images with the captured images and to implement system parameter calibration. The phase recovery and improved resolution of experimental images show that the new algorithm produces good recovery for object amplitude and phase as well as the pupil aberrations for wide field imaging. The pupil vignetting of the optics limits the maximum FoV that can be successively imaged and recovered in the FPM scheme.

Declaration of competing interest

The authors declare that they have no known competing financial interests or personal relationships that could have appeared to influence the work reported in this paper.

Appendix. Pseudo-MATLAB code

The Fresnel propagation based FP algorithm is given here as a pseudo-MATLAB code, which is based on the FP algorithm with complex-pupil recovery (Zheng, 2016; Tian and Waller, 2015; Manuel Guizar-Sicairos and Fienup, 2008).

```
Define x, y coordinates for LEDs,
sensor pixel size spsize,
High-resolution pixel size psize,
image patch center ox, oy
Define z1, z2, zled, Lens_diameter
Define axis array on object OX,OY
and Lens plane LX, LY
Discretization distance on Lens plane Ldx,Ldy
Low resolution matrix size m1 x n1
High resolution matrix size m x n
Define Pupil_Amplitude, matrix size m1 x m1
Read images, do noise removal
and background removal,
Calibrate LED misplacement and rotation
Calibrate z1, ox, oy and Pupil diameter
objectRec=upscaled bright-field image size mxm;
ELens_FT=FFT(objectRec.*exp(j*k/2/z1*(OX.^2+OY.^2).
*exp(j*k/2/zled*(OX.^2+OY.^2)));
Pupil_Rec = Pupil_Amplitude; % Unknown complex pupil guess

for loop=1:1:max_itertions
for LED_no=1:1:end
% amount of shift for off-axis LED
s_x=((x_LED(LED_no)-ox)/L*z1-ox)/Ldx;
s_y=((y_LED(LED_no)-oy)/L*z1-oy)/Ldx;
% shift center, in pixels
kxc=round((n/2+1)+s_x);
kyc=round((m/2+1)+s_y);
% lower and upper limit of shifted pupil
kxl=round(kxc-n1/2);
kxh=round(kxc+n1/2-1);
kyl=round(kyc-m1/2);
kyh=round(kyc+m1/2-1);
% selected field at the Lens plane,
LowResFT1=Pupil_Rec .* ELens_FT(kyl:kyh,kxl:kxh);
% Forward image model
ImLowRes=IFT(LowResFT1);
% Replace with recorded amplitude
ImLowRes=sqrt(Image(LED_no)).*exp(j*angle(ImLowRes));
% Back to lens plane
LowResFT2=(m/m1)^2*FFT(ImLowRes);
% Update the sub-spectrum at Lens plane
ELens_FT(kyl:kyh,kxl:kxh)=LowResFT1+abs(Pupil_Rec).*
conj(Pupil_Rec)./max(max(abs(Pupil_Rec)))
./(abs(Pupil_Rec).^2+1.0).*(LowResFT2-LowResFT1);
% Update the complex pupil
Pupil_Rec=Pupil_Rec+abs(lowResFT1).*conj(LowResFT1.*Pupil_Ampl)./
max(max(abs(LowResFT1)))
./(abs(LowResFT1).^2+1000.0).*(LowResFT2-LowResFT1);
end
end
% Propagate full field matrix back to lens plane
% Final high resolution complex recovered object
objectRecover=exp(-j*k/2/zled*(OX.^2+OY.^2).*
exp(-j*k/2/z1*(OX.^2+OY.^2)).
*IFT(ELens_FT);
```

References

Bian, Z., Dong, S., Zheng, G., 2013. Adaptive system correction for robust Fourier ptychographic imaging. Opt. Express 21 (26), 32400–32410.

Eckert, R., Phillips, Z.F., Waller, L., 2018. Efficient illumination angle self-calibration in Fourier ptychography. Appl. Opt. 57 (19), 5434–5442.

Goodman, J.W., 2017. Introduction to Fourier Optics, fourth ed. W. H. Freeman, ISBN: 978-1319119164.

Guo, K., Dong, S., Zheng, G., 2016. Fourier ptychography for brightfield, phase, darkfield, reflective, multi-slice, and fluorescence imaging. IEEE J. Sel. Top. Quantum Electron. 22 (4), 6802712.

Konda, P.C., 2017. Multi-Aperture Fourier Ptychographic Microscopy: Development of a High-Speed Gigapixel Coherent Computational Microscope (Ph.D. thesis). University of Glasgow: School of Physics and Astronomy College of Science and Engineering.

Konda, P.C., Loetgering, L., Zhou, K.C., Xu, S., Harvey, A.R., Horstmeyer, R., 2020. Fourier ptychography: current applications and future promises. Opt. Express 28 (7), 9603–9630.

Liu, J., Li, Y., Wang, W., Zhang, H., Wang, Y., Tan, J., Liu, C., 2017. Stable and robust frequency domain position compensation strategy for Fourier ptychographic microscopy. Opt. Express 25 (23), 28053–28067.

Manuel Guizar-Sicairos, M., Fienup, J.R., 2008. Phase retrieval with transverse translation diversity: a nonlinear optimization approach. Opt. Express 16 (10), 7264–7278.

Ou, X., Horstmeyer, R., Zheng, G., Yang, C., 2015. High numerical aperture Fourier ptychography: principle, implementation and characterization. Opt. Express 23 (3), 3472–3491.

Ou, X., Zheng, G., Yang, C., 2014. Embedded pupil function recovery for Fourier ptychographic microscopy. Opt. Express 22 (5), 4960–4972.

Pan, A., Zhang, Y., Zhao, T., Dan, D., Lei, M., Yao, B., 2017. System calibration method for Fourier ptychographic microscopy. J. Biomed. Opt. 22 (9), 096005–096011.

Pan, A., Zuo, C., Xie, Y., Zhang, Y., Lei, M., Yao, B., 2019. Vignetting effect in Fourier ptychographic microscopy. Opt. Lasers Eng. 120, 40–48.

Sun, J., Chen, Q., Zhang, Y., Zhu, C., 2016. Efficient positional misalignment correction method for Fourier ptychographic microscopy. Opt. Express 7 (4), 1336–1350.

Sun, J., Zuo, C., Zhang, J., Fan, Y., Chen, Q., 2018. High-speed Fourier ptychographic microscopy based on programmable annular illuminations. Sci. Rep. 8 (1), 7669.

Tian, L., Waller, L., 2015. 3D intensity and phase imaging from light field measurements in an LED array microscope. Optica 2 (2), 104–111.

Wang, Z., Bovik, A.C., Sheikh, H.R., Simoncelli, E.P., 2004. Image quality assessment: from error visibility to structural similarity. IEEE Trans. Image Process. 13 (4), 600–612.

Zhang, Y., Pan, A., Lei, M., Yao, B., 2017. Data preprocessing methods for robust Fourier ptychographic microscopy. Opt. Eng. 56 (12), 123107–1231013.

Zheng, G., 2014. Breakthroughs in photonics 2013: Fourier ptychographic imaging. IEEE Photonics J. 6 (2).

Zheng, G., 2016. Fourier Ptychographic Imagig: A MATLAB Tutorial. Morgan and Claypool, ISBN: 978-1-6817-4273-1.

Zhou, A., Wang, W., Chen, N., Lam, E.Y., Lee, B., Situ, G., 2018. Fast and robust misalignment correction of Fourier ptychographic microscopy for full field of view reconstruction. Opt. Express 26 (18), 23661–23674.